American Mineralogist, Volume 86, pages 456–465, 2001

$Fe^{3+}/\Sigma Fe$ vs. Fe$L\alpha$ peak energy for minerals and glasses: Recent advances with the electron microprobe

MICHEL FIALIN,[1,*] CHRISTIANE WAGNER,[2] NICOLE MÉTRICH,[3] ERIC HUMLER,[4] LAURENCE GALOISY,[5] AND ANTOINE BÉZOS[4]

[1]Centre de Microanalyse Camparis-CNRS, Université Paris 6, 4 place Jussieu, 75252 Paris cedex 5, France
[2]Laboratoire de Pétrologie, Modélisation des Matériaux et Processus, Université Paris 6, 4 place Jussieu, 75252 Paris cedex 5, France
[3]Laboratoire Pierre Süe, UMR 9956-CNRS, CE-Saclay, 91191 Gif sur Yvette, France
[4]Laboratoire de Géosciences Marines-CNRS, Université Paris 6 et 7, Institut de Physique du Globe, 4 place Jussieu, 75252 Paris cedex 5, France
[5]Laboratoire de Minéralogie-Cristallographie, UMR 7590-CNRS, Universités Paris 6 et 7, Institut de Physique du Globe, 4 place Jussieu, 75252 Paris cedex 5, France

ABSTRACT

This paper describes a preliminary study that attempts to determine the oxidation state of Fe ($Fe^{3+}/\Sigma Fe$) with the electron microprobe (EMP) by measuring the self-absorption induced shift of the Fe$L\alpha$ peak emitted from minerals and glasses. In transition metals of the first row, the L-spectra exhibit common distortions, namely peak position shifts, peak shape alterations, and changes in the $L\beta/L\alpha$ ratios, caused by the large difference in the self-absorption coefficients (μ/ρ) on either sides of the L_3 absorption edges that are in close proximity to the $L\alpha$ peak maxima. Measurements performed on α-Fe_2O_3 and Fe_xO oxides have shown that self-absorption effects are stronger for the later oxide, leading to enhanced $Fe^{2+}L\alpha$ peak shift toward longer wavelengths as the beam energy increases. First measurements performed on silicates have confirmed that enhanced self-absorption of Fe$L\alpha$ occurs on Fe^{2+} sites. The measurements consisted of plotting the Fe$L\alpha$ peak position at a fixed beam energy (15 keV) against the total Fe concentration for two series of Fe^{2+}- and Fe^{3+}-bearing silicates. In a first step, these data have shown that both $Fe^{2+}L\alpha$ and $Fe^{3+}L\alpha$ peaks shift continuously toward longer wavelengths as the Fe concentration increases, with enhanced shifts for $Fe^{2+}L\alpha$. For silicates containing only Fe^{2+} or Fe^{3+}, no effects of the site geometry were detected on the variations of the Fe$L\alpha$ peak position. A second set of plots has shown the variations of the peak position relative to the previous Fe^{2+}-Fe^{3+} curves of step 1, as a function of the nominal $Fe^{3+}/\Sigma Fe$, for a series of reference minerals (hydrated and non-hydrated) and basaltic glasses. Data from chain and sheet silicates (e.g., pyroxenes, amphiboles, micas) exhibited strong deviations compared to other phases (e.g., garnets, Al-rich spinels, glasses), due to reduced self-absorption of Fe$L\alpha$. Intervalence-charge transfer (IVCT) mechanisms between Fe^{2+} and Fe^{3+} sites may be the origin of these deviations. These crystal-structure effects limit the accuracy of the method for mixed Fe^{2+}-Fe^{3+} valence silicates. Precisions achieved for further $Fe^{3+}/\Sigma Fe$ measurements strongly depend on the total Fe concentration. For basaltic glasses containing an average of 8 wt% Fe and 10% $Fe^{3+}/\Sigma Fe$, the precision is about ±2% (absolute). For low Fe concentrations (below 3.5 wt%), the uncertainty in the peak position measured by the EMP spectrometers leads to error bars that are similar to with the separation of the curves fitted to the Fe^{2+} and Fe^{3+} plots, which is propagated as prohibitive lack of precision for $Fe^{3+}/\Sigma Fe$ (>70% relative). A major limitation of microbeam methods in general deals with beam damage. This aspect has been carefully studied for basaltic glasses, and optimal beam conditions have been established (in general, electron doses higher than those corresponding to 130 nA and 30 μm beam diameter should be avoided to prevent large beam induced oxidation phenomena). Additional work, in progress, concerns: (1) other beam-sensitive phases such as hydrated glasses; and (2) minerals in which Fe$L\alpha$ is affected by large matrix effect corrections (e.g., Cr- and Ti-rich oxides where Fe$L\alpha$ is strongly absorbed), for which the self-absorption-induced shift of Fe$L\alpha$ is different from that of common silicates and glasses.

INTRODUCTION

The redox state of Earth's mantle is a critical parameter to constrain models on the origin and the evolution of the Earth. Oxygen fugacity plays an important role in volatile speciation, physical properties of mantle rocks, core-mantle interactions, and the atmospheric chemistry through time (Kadik and Lukanin 1985; Kasting et al. 1993). The redox state of the upper mantle is commonly estimated through values of oxygen fugacity calculated on the basis of Fe^{2+}/Fe^{3+} equilibrium among mineral assemblages such as olivine-orthopyroxene-spinel (Ballhaus et al. 1990; O'Neill et al. 1993) or determined by

* E-mail: fialin@ccr.jussieu.fr

wet chemical analyses on minerals or glasses (Christie et al. 1986). For example, systematic relationships have been pointed out between upper mantle oxidation states and tectonic regimes (e.g., Wood et al. 1990; Canil et al. 1994). However, the effects of different processes on mantle redox conditions are still debated: are the large variations in the redox state linked to C-O-H fluids (Mattioli et al. 1989) or do they result only from magmatic processes, partial melting, and melt infiltration (Amundsen and Neumann 1992; McGuire et al. 1991)? Many of the controversies about this subject ultimately relate to the paucity and irrelevance of the available data. This lack of data may be the major justification for continuing to search for techniques of determining $Fe^{3+}/\Sigma Fe$.

Iron commonly occurs in two different oxidation states. The redox state of Fe is strongly dependent on the interaction with C-O-H fluids in natural magmas. These fluids play quite different structural roles (Waychunas et al. 1988; Cooney and Sharman 1990; Jackson et al. 1990) and have considerable influence on properties of silicate melts such as density or viscosity. The effect of the oxidation state of Fe and oxygen, the changes in $Fe^{3+}/\Sigma Fe$, and interactions of Fe and O in silicate melts have been widely debated (e.g., Dyar 1985; Mysen 1988). The determination of $Fe^{3+}/\Sigma Fe$ along with the sites occupied by Fe^{3+} and Fe^{2+}cations and their relationships with the silicate framework provide a basis from which the thermal history, and hence the melting processes by which a particular natural glass has formed, may be deduced.

Different methods are commonly used to measure $Fe^{3+}/\Sigma Fe$ in silicates and glasses and will be briefly reviewed in the next section. Extracting quantitative $Fe^{3+}/\Sigma Fe$ values from the Fe$L\alpha,\beta$ emission spectra measured with the EMP has been a long-term subject of study in geological applications (see Höfer et al. 1994 for a history of the related works over the past 35 years). Actually three ways have been investigated to process the Fe-$L\alpha,\beta$ spectra: (1) measurement of the $L\alpha$ peak shifts; (2) measurement of the change in $L\beta/L\alpha$ intensity ratios; and (3) a hybrid of 1 and 2 (Höfer et al. 1994, 2000).

We present in this study a technique based on method (1) that is applicable to minerals and glasses for which the total Fe concentration (in wt%) has been previously established. The limitations of the method are discussed.

Existing methods for the determination of $Fe^{3+}/\Sigma Fe$

Bulk methods

Several bulk methods have been developed to determine Fe^{2+} in silicate minerals. (1) Volumetric and colorimetric methods were proposed by Wilson (1960). Decomposition of the sample is carried out at room temperature by hydrofluoric acid containing V^{5+} to oxidize Fe^{2+} as it passes into solution. Between 50 and 200 mg of carefully hand-picked glass is required for this method. (2) Electrochemical cells (e.g., Sato 1970; Kadik 1997) also may be used for measuring oxygen fugacities, but reduction of the Fe^{3+} during experiments with C-bearing samples provides low f_{O_2} values (Virgo et al. 1988). (3) In Mössbauer spectroscopic analysis, $Fe^{3+}/\Sigma Fe$ can be determined directly from the relative areas of the Fe^{3+} and Fe^{2+} quadrupole split doublets. A major advantage of the technique is that any uncertainty in the total Fe content of the sample does not affect the $Fe^{3+}/\Sigma Fe$, because the Mössbauer spectroscopy involves only deconvolution of the spectral data. In contrast, large uncertainties occur when $Fe^{3+}/\Sigma Fe$ is so low that the high-velocity component of the Fe^{3+} doublet is no longer discernible in the spectral data. This is usually the case for phases with less than 10% Fe^{3+} (i.e., $Fe^{3+}/\Sigma Fe < 0.1$). In addition, the spectra of amorphous solids are less well defined than those of their crystalline analogs (e.g., Mao et al. 1973; Eibschutz and Lines 1982), which introduces some uncertainties in the least-squares fitting used for the deconvolution procedure. (4) Millimetric X-ray beams, and related X-ray photoelectron spectroscopy or XPS, can be used by analyzing the Fe^{2+} and Fe^{3+} photopeaks emitted from the sample (Raeburn et al. 1997a, 1997b). Owing to the low escape depth of the photoelectrons (typically 5 nm) the method is very surface sensitive, which requires enhanced sample preparation to prevent surface contamination. Very low $Fe^{3+}/\Sigma Fe$ (down to 2%) can be measured by this method with uncertainties below ±10% relative. (5) Crystal field absorption spectroscopy with millimetric near-IR-visible-UV sources gives information on the oxidation state, coordination number, and geometry of the cation sites by processing the $d \rightarrow d$ transitions in the UV-visible region (200 nm) (Burns 1993). In theory, the intensity of the absorption bands allows the researcher to determine the concentration of the cation in its various oxidation states using the Beer-Lambert relationship (e.g., Bingham et al. 1999). For Fe, however, measurement of the Fe^{3+} band, of low intensity compared to Fe^{2+}, is rendered difficult by the presence of an intense absorption background due to intervalence charge transfer (IVCT) between Fe^{2+} and Fe^{3+} cations (Fe^{2+} 3d $\rightarrow$ Fe^{3+} 3d transitions, below for more comments on IVCT mechanisms).

The major criticism against bulk methods concerns the purity of the samples. Even carefully hand-picked glasses or minerals may contain traces of some other material that significantly changes the $Fe^{3+}/\Sigma Fe$ value.

Microbeam methods

To avoid contributions from undesirable phases, micro-beam techniques are particularly useful. Selection of surfaces from natural glasses or minerals that are free of any alteration, cracking, or secondary veins can be made by optical examination even at a scale of about 5 μm. Furthermore, these techniques are also useful for experimental materials, with dimensions ranging from few hundred micrometers to few millimeters, which cannot be processed by the common bulk methods cited above. Finally, it is important to emphasize that, unlike bulk methods, a quantity of about 1 μg can in theory be processed using microbeams. The Mössbauer method has been adapted to the study of samples with an area as small as 100 μm^2 with the development of the milliprobe (McCammon et al. 1991). The main disadvantage of the later method is the long time exposures required to balance the weak intensity of the beam.

The local determination of the oxidation states of Fe using both electron and X-ray spectroscopies has become more and more popular as a consequence of the development of modern micro-beam sources (electrons or X-rays). Active research on

synchrotron-based, high-resolution micro-XANES (X-ray near edge absorption structure) at Fe*K*- and *L*-edges is in progress in connection with computer simulations to provide information on chemical bonding and oxidation states (Cressey et al. 1993; de Groot 1994; Brown et al. 1995; Westre et al. 1997; Delaney et al. 1998). This method promises to provide information on oxidation states and site occupancy of Fe in magmas where data for both remain controversial. Dramatic increase of the spatial resolution has been achieved by the development in the transmission electron microscope of ELNES (energy-loss near-edge structure spectroscopy), the equivalent of XANES for electrons, which allows the determination of $Fe^{3+}/\Sigma Fe$ at the 10 nm scale by probing the Fe*L*- and *M*-edges (van Aken et al. 1998, 1999; Garvie and Buseck 1998). For the EMP, $Fe^{3+}/\Sigma Fe$ can be determined by Höfer's technique (cited above) using calibration curves constructed from precise measurements on reference materials. Using separate calibration curves for each mineral group, the precision and accuracy of $Fe^{3+}/\Sigma Fe$ with this later method is 2% (absolute).

Experimental methods

Instrumentation

Measurements were carried out with a Cameca Camebax EMP, operating at 15 keV, using TAP monochromator crystals ($2d$ = 2.575 nm). The Fe$L\alpha$ peak maximum was located by using the regular automatic routine of the Cameca EMP software. The time required for a single peak search was 60 s, leading to an uncertainty of about ±8 Bragg sin angle ($\sin\theta$) increments (1 increment = 1.10^{-5} $\sin\theta$) in the Fe$L\alpha$ peak position for Fe concentrations ranging 5 to 30 wt% with a beam current of 40 nA. The pulse height analyzer was set to avoid the interference of Fe$L\alpha$ with the high-energy ninth-order Fe$K\alpha$ peak.

Sample description

The method for determining $Fe^{3+}/\Sigma Fe$ is based on two calibration stages, for which two specific groups of both hydrous and anhydrous minerals have been selected, together with natural and synthetic glasses. For the first calibration stage, the following anhydrous minerals containing either Fe^{2+} or Fe^{3+} were selected: (1) *clinopyroxenes* (diopside and hedenbergite, with 3 and 16 wt% Fe^{2+} respectively, and acmite with 19 wt% Fe^{3+}); (2) *orthopyroxene* with 9 wt% Fe^{2+}, (3) *olivines* with 3–17 wt% Fe^{2+}; (4) *garnets* (andradite with 22 wt% Fe^{3+} and almandine with 17 wt% Fe^{2+}); (5) *K-feldspar* with 4 wt% Fe^{3+}; (6) *epidote* with 7 wt% Fe^{3+}; and (7) *staurolite* with 9.9 wt% Fe^{3+}.

For the second calibration stage, samples with varying $Fe^{3+}/\Sigma Fe$ have been selected. Mineral species were (1) *clinopyroxenes* (six minerals) with 5–23 wt% Fe and 15–96% $Fe^{3+}/\Sigma Fe$; (2) *garnets* (four minerals) with 5–20 wt% Fe and 47–90% $Fe^{3+}/\Sigma Fe$; (3) *Al-rich spinels* (seven minerals) with 9–17 wt% Fe and 14–75% $Fe^{3+}/\Sigma Fe$; (4) *amphiboles* (two minerals) with 7–10 wt% Fe and 95–98% $Fe^{3+}/\Sigma Fe$; (5) *micas* (four minerals) with 8–18 wt% Fe and 15–33 $Fe^{3+}/\Sigma Fe$. The following 25 glass samples also were studied: (1) *tholeiitic* (16 natural samples) with 7–10 wt% Fe and 10–17% $Fe^{3+}/\Sigma Fe$; (2) *basaltic lava* (six samples obtained by fusion of powdered natural glasses at 1270–1300 °C under controlled air fluxes to obtain the required $Fe^{3+}/\Sigma Fe$) with 6–8 wt% Fe and 30–85% $Fe^{3+}/\Sigma Fe$; and (3) *andesitic* (three synthetic samples, same treatment as for the basaltic glasses) with 5–16 wt% Fe and 50–64% $Fe^{3+}/\Sigma Fe$. The essential data on mineral and glass compositions used in this study are presented in Table 1. Values of $Fe^{3+}/\Sigma Fe$ were either calculated by common stoichiometry and charge-balance relationships deduced from EMP analyses of anhydrous minerals, or measured by wet chemistry and/or Mössbauer spectroscopy for glasses (Humler et al. 1998; Neuville et al., unpublished data, 1999) and hydrous silicates (wet chemistry on separated minerals).

Self-absorption of low energy $L\alpha$ peaks

The *L*-series peaks emitted from the first row transition metals are the result of radiative electronic transitions between the partially filled 3d orbitals to the 2p (or $L_{2,3}$) core levels. The energies of these peaks are below 1 keV. Several papers have described the *L*-series of light transition metals, as well as those of Cu and Zn (Parratt 1959; Holliday 1968; Bonnelle 1987), and point out the large contribution of self-absorption (i.e., absorption by its own atoms or ions of X-ray photons emitted from a chemical species) in misinterpretation of experimental spectra. Indeed, self-absorption is responsible for asymmetries on the high-energy side of the *L*-peaks, leading to peak position shifts and changes in the $L\beta/L\alpha$ ratio (O'Nions and Smith 1971; Rémond et al. 1996). These spectral distortions are caused by the large contrasts in absorption coefficients on either side of the metal L_3 edges that are in close proximity to the $L\alpha$ peak maxima. The full widths at half maximum (FWHM) of low-energy *L* peaks is the convolution of the natural widths of both 3d and 2p levels. The energy distributions of the 2p levels are described by Lorentzian curves with widths inversely proportional to the lifetime of the 2p-core holes. The 2p level width is ~1.5 eV in Fe (Bonnelle 1966). In addition, the final state hole causes the 3d band to broaden. Similar peak broadenings related to the lifetime of the ionized state affect the 2p absorption spectra (de Groot et al. 1990). Self-absorption occurs when lifetime broadenings are large enough to initiate overlap between both emission and absorption bands. Due to the later intrinsic loss of resolving power of the method, photons are generated with the minimal energy required for transitions from the 2p core level to continuum states (empty states just above the Fermi level, E_F, for low energy peaks). Empty states at E_F for transition metals are composed of admixtures of 3d and 4sp states. In applying dipole selection rules, transitions of core electrons (as 2p electrons) to localized empty states (e.g., 3d) dominate over delocalized conduction states (e.g., 4sp). Both types of transitions may dramatically change the shape of the L_3-edge with strong effects on the self-absorption. A classical example is given by the comparison of the CuL_3 absorption spectra of Cu_2O and CuO (e.g., Bonnelle 1966). The L_3 discontinuity of the former is arctangent shaped, which is characteristic of 2p $\rightarrow$ 4s transitions (low self-absorption of Cu$L\alpha$), whereas that of the later consists of a white-line (i.e., is peak shaped) as a consequence of highly probable transitions to the 3d-hole localized on the e_g orbital (high self-absorption of Cu$L\alpha$). Therefore, the self-absorption intensity of soft $L\alpha$ peaks

TABLE 1. Complete table of the mineral and glass compositions used in this study; electron microprobe chemical analyses in wt%

	Px	Px	Px	Px	Px	Gt
SiO_2	52.53	52.06	51.86	48	49.05	28.4
TiO_2	4.31	1.15	6.03	1.14	0	12.23
Al_2O_3	1	0.04	0.65	4.83	0.64	3.16
FeO(total)	23.58	29.52	19.05	13.31	23.98	18.05
MnO	2.73	0.12	0.1	0.46	3.14	0.33
MgO	0.34	0.02	4.07	8.47	0.73	1.26
CaO	0.37	0	4.42	20.7	22.14	32.36
Na_2O	13.37	13.99	11.05	1.69	0	0.03
K_2O	0	0	0	0	0	0
Total	98.23	96.9	97.23	98.6	99.68	95.82
$Fe^{3+}/\Sigma Fe(\%)$	97	94	83	36	0	96
	Gt	Gt	Gt	Gt	Ol	Ol
SiO_2	33.22	38.02	37.89	39.28	42.04	41
TiO_2	4.98	0.05	0.05	0	0	0
Al_2O_3	1.93	18.66	18.37	22.22	0	0.03
FeO(total)	23.6	6.65	8.45	22.05	3.08	7.08
MnO	0.74	13.62	13.78	0.48	0	0.1
MgO	0.26	0.05	0.06	11.38	54.53	51.9
CaO	31.14	22.48	20.83	4.2	0	0
Na_2O	0.14	0	0	0	0	0
K2O	0	0	0	0	0	0
Total	98.36	99.5	99.43	99.61	99.65	100.1
$Fe^{3+}/\Sigma Fe(\%)$	90	63	47	0	0	0
	Ol	Ol	Ol	Ol	K-fp	epidote
SiO_2	40.78	39.8	39.2	38.2	64.52	38.64
TiO_2	0	0.03	0.02	0	0.49	0
Al_2O_3	0	0.07	0.06	0.05	13.51	24.26
FeO(total)	9.57	11.7	13.5	17.2	4.31	8.96
MnO	0.19	0.14	0.18	0.21	0	0
MgO	49.2	47.9	46.4	43.4	0.09	0
CaO	0	0.14	0.1	0	0.06	23.93
Na_2O	0	0	0	0	0.54	0
K_2O	0	0	0	0	15.63	0
Total	99.74	99.78	99.46	99.06	99.15	95.79
$Fe^{3+}/\Sigma Fe(\%)$	0	0	0	0	100	100
	spinel*	spinel*	spinel*	spinel*	spinel*	spinel*
SiO_2	0	0	0	0	0	0
TiO_2	0.19	0.24	0.14	0.31	0.08	0.19
Al_2O_3	59.99	60.85	60.83	62.78	64.09	59.47
FeO(total)	11.84	12.66	22.71	16.96	17.01	21.36
MnO	0.1	0.16	0.14	0.14	0.17	0.11
MgO	24.48	22.84	15.38	18.28	18.22	14.59
CaO	0	0	0	0	0	0
Na_2O	0	0	0	0	0	0
K_2O	0	0	0	0	0	0
Total	96.6	96.75	99.2	98.47	99.57	95.72
$Fe^{3+}/\Sigma Fe(\%)$	75	56	25	19	17	17
	spinel*	Amp	Amp	mica	mica	mica
SiO_2	0	38.58	38.43	35.83	34.5	34.45
TiO_2	0.61	4.89	4.85	5.51	2.5	2.02
Al_2O_3	60.36	14.72	14.64	16.37	17.51	20.39
FeO(total)	19.57	11.54	13.34	10.02	24.12	23.51
MnO	0.13	0.09	0.13	0.06	0.96	0.64
MgO	16.1	12.31	11.36	17.03	6.15	2.1
CaO	0	11.01	10.85	0.22	0.1	0.01
Na_2O	0	2.4	2.38	0.7	0.03	0.06
K_2O	0	1.47	1.35	9.04	8.73	8.99
Total	96.77	97.01	97.33	94.78	94.6	93.17
$Fe^{3+}/\Sigma Fe(\%)$	14	98	90	33	24	15

	mica	St.	tholeiitic	tholeiitic	tholeiitic	tholeiitic
SiO_2	36.69	28.67	51.36	50.21	48.62	49.88
TiO_2	1.63	0.58	1.89	1.62	0.91	1.27
Al_2O_3	18.4	55.57	13.86	16.29	17.52	17.37
FeO(total)	15.73	12.75	12.32	8.44	9.06	7.29
MnO	0.04	0.28	0.2	0.16	0.18	0.13
MgO	12.36	1.66	6.69	7.67	9.25	8.1
CaO	0.02	0	10.69	9.92	10.42	9.9
Na_2O	0.51	0	2.1	3.87	3.09	3.89
K_2O	8.91	0	0.21	0.19	0.05	0.26
Total	94.3	99.51	99.32	98.37	99.05	97.83
$Fe^{3+}/\Sigma Fe(\%)$	15	100	15	15	12	16
	tholeiitic	tholeiitic	tholeiitic	tholeiitic	tholeiitic	tholeiitic
SiO_2	50.01	49.5	50.62	49.85	49.44	50.28
TiO_2	2.14	1.25	1.8	1.55	1.38	1.63
Al_2O_3	15.1	15.06	13.92	16.15	16.75	16.13
FeO(total)	10.51	10.66	11.34	8.62	7.88	8.64
MnO	0.2	0.2	0.23	0.17	0.15	0.16
MgO	6.76	7.8	6.49	8.03	8.06	7.79
CaO	9.82	11.28	10.64	10.27	10.26	9.76
Na_2O	3.77	2.56	2.92	3.56	3.62	3.82
K_2O	0.23	0.05	0.29	0.17	0.2	0.23
Total	98.54	98.36	98.25	98.37	97.74	98.44
$Fe^{3+}/\Sigma Fe(\%)$	10	12	15	14	14	18
	tholeiitic	tholeiitic	tholeiitic	tholeiitic	B-lava	B-lava
SiO_2	50.06	50.53	48.5	49.64	47.4	49.68
TiO_2	1.21	1.33	1.3	1.72	1.6	0.92
Al_2O_3	17.07	16.77	16.82	13.32	14.9	18.56
FeO(total)	8.66	7.64	9.48	13.49	10.1	7.13
MnO	0.16	0.1	0.13	0.23	0.12	0.16
MgO	7.92	7.7	8.4	6.48	7.4	5.42
CaO	10.09	9.89	9.87	10.52	12.2	10.38
Na_2O	3.56	3.89	2.96	2.68	2.5	2.58
K_2O	0.19	0.24	0.03	0.2	1.3	2.2
Total	98.92	98.09	97.49	98.28	97.52	97.04
$Fe^{3+}/\Sigma Fe(\%)$	16	15	11	15	85	74
	B-lava	B-lava	B-lava	B-lava	andesitic	andesitic
SiO_2	47.68	50.18	47.74	47.66	54.06	48.5
TiO_2	1.75	0.96	1.76	1.74	0.43	0.5
Al_2O_3	18.57	17.96	17.89	18.35	17.56	15.76
FeO(total)	9.76	7.42	9.87	9.89	11.79	20.95
MnO	0.19	0.16	0.18	0.2	0	0
MgO	5.26	5.85	5.48	5.41	2.83	2.48
CaO	10.03	1065	10.15	10.08	8.12	7.27
Na_2O	3.8	2.58	3.74	3.69	3.12	2.72
K_2O	1.84	2.2	1.83	1.79	0.8	0.89
Total	98.88	97.97	98.64	98.8	98.71	99.07
$Fe^{3+}/\Sigma Fe(\%)$	56	36	34	24	64	58
	andesitic					
SiO_2	62.75					
TiO_2	0.44					
Al_2O_3	19.55					
FeO(total)	6.72					
MnO	0					
MgO	3.06					
CaO	3.8					
Na_2O	1.6					
K_2O	0.41					
Total	98.33					
$Fe^{3+}/\Sigma Fe(\%)$	50					

Notes: Px = pyroxene; Gt = garnet; K-fp = K-feldspar; St = staurolite; B-lava = Basaltic lava glasses.
* Al-rich spinel.

is tightly related to both density and spatial extension of empty 3d at E_F and to the rate of 3d-4sp hybridization, or mixing, as well. In oxides, metal 3d and oxygen 2p states are more or less mixed, which imparts some p-character to the 3d wave functions, thus reducing the $2p \rightarrow 3d$ transition probability. In summary, the lower the density of unmixed 3d states at E_F, and the lower their localized character, the lower the self-absorption intensity. The self-absorption of low energy *L* peaks is thus very sensitive to the nature and the arrangement of the lattice surrounding the absorbing atoms.

The attenuation by self-absorption of the Lα photons along their path to the surface of a bulk material is described by:

$$I/I_0 = \exp(-C \cdot \mu/\rho \cdot \rho z \cdot \mathrm{cosec}\theta) \quad (1)$$

where I_0 is the intensity generated at mass depth ρz, *I* is the

emerging intensity, *C* is the weight fraction (wt%) of the metal, μ/ρ is the mass self-absorption coefficient (sensitive to structural and chemical effects, as discussed above), and θ is the take-off angle. Larger self-absorption-induced distortions of *L*α peaks are produced at high beam energy and high metal abundance, related to parameters ρz and *C* in Equation 1, respectively.

The Fe*L*α peak positions for Fe_2O_3 (hematite) and $Fe_{0.94}O$ (wüstite, referred to as FeO in the text) are plotted against beam energy in Figure 1 indicating larger self-absorption effects in the later. First, the Fe^{2+} peak position measured at any fixed beam energy is systematically shifted toward larger sinθ compared with Fe^{3+}. Second, the Fe^{2+}-Fe^{3+} peak separation increases as the beam energy increases to reach the large value of approximately 100 sinθ increments at 15 keV. Extrapolation of the peak positions to the FeL_3 edge energy, where self-absorption is eliminated, shows reduced *L*α peak shift. Figure 2 shows the self-absorption spectra recorded with the EMP at the FeL_3 edge of Fe_2O_3 and FeO. These spectra were constructed by taking point by point ratios of two *L*α peaks, one of which was measured at 2 keV and thus was weakly distorted by self-absorption, whereas the other was measured at 10 keV and was strongly altered by it. This method was described by Liefeld (1968) as an easy way to extract self-absorption data of low transition metals from bulk specimens analyzed with an electron beam. The reduced height together with the shift in energy (ca. 1.3 eV) of the absorption maximum of Fe_2O_3 compared with FeO is in good agreement with the calculated L_3 absorption spectra closest to E_F for Fe^{3+} and Fe^{2+} in octahedral symmetry, the actual coordination of both ions in Fe_2O_3 and FeO, respectively (Cressey et al. 1993). Also indicated in Figure 2 are the extrapolated positions of the Fe*L*α peak maxima, as deduced from Figure 1, which shows the enhanced overlap of both absorption and emission bands for FeO.

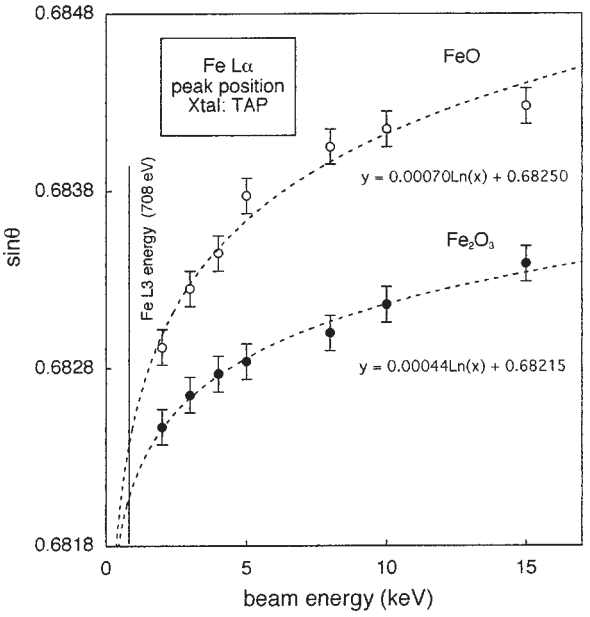

FIGURE 1. Fe*L*α peak position (sin units) as a function of the beam energy (2, 3, 4, 5, 8, 10, and 15 keV) for FeO and Fe_2O_3. Extrapolation of plots through the given Ln curves to the critical excitation voltage for FeL_3 (708 eV) show reduced peak shift for both oxides: sin = 0.68200 for Fe O and sin = 0.68226 for FeO. Error bars are given for an uncertainty of ± 8 sin increments on the Fe*L*α peak position. Due to technological limitations, beam energies below 2 keV were not available with the EMP of the study.

SPECIATION OF IRON IN MINERALS AND GLASSES

Methodology

To evaluate the contribution of Fe concentration to self-absorption effects, the Fe*L*α peak shift measured at 15 keV (the common beam energy used in geological applications) was plotted in Figure 3 vs. wt% Fe for a series of almost pure Fe^{2+}- and Fe^{3+}-bearing silicates. The continuous peak shift observed toward larger wavelengths for Fe^{2+} is consistent with increasing self absorption as wt% Fe increases. The few data collected for Fe^{3+} compounds show a trend similar to Figure 1: given the level of self absorption—fixed by the wt% Fe in Figure 3—the Fe^{3+} peak is shifted toward shorter wavelengths compared with Fe^{2+}. The Fe^{3+}-Fe^{2+} peak separation is as large as 160 sinθ increments at 20 wt% Fe and is reduced to 30 sinθ increments at 3.5 wt% Fe. It should be noted that, despite the change in the coordination number of Fe^{2+} ions, which ranges from sixfold (octahedral) in pyroxenes and olivines to eightfold (cubic) in garnets to fourfold (tetrahedral) in staurolite, no obvious anomaly is noted on the plots in Figure 3. The same remark holds for the Fe^{3+} curve that has been constructed with minerals where Fe^{3+} is sixfold coordinated, except in feldspar where it is fourfold coordinated. These results show that no effects of

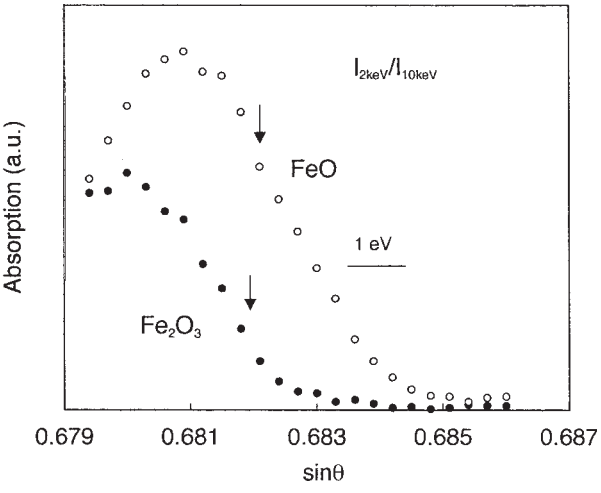

FIGURE 2. Experimental self-absorption spectra (L_3 edge) for FeO and Fe_2O_3 resulting from the intensity ratio of the Fe*L*α spectra measured at 2 and 10 keV beam energy, respectively. The shift between both absorption peaks is ~1.3 eV. Arrows indicate the Fe*L*α peak maxima for FeO and Fe_2O_3 extrapolated to the critical excitation voltage for FeL_3, as deduced from Figure 1: $Fe^{2+}L$ experiences more self-absorption than $Fe^{3+}L$ as a result of enhanced overlap of both emission and absorption L_3 bands for FeO (a.u. = arbitrary units).

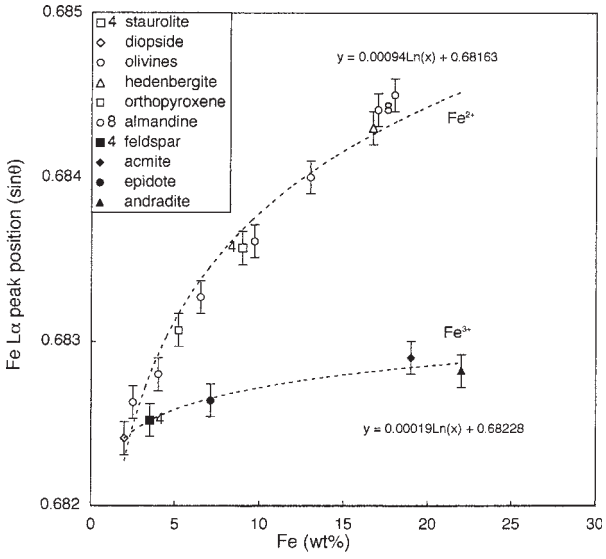

FIGURE 3. Variations of the Fe$L\alpha$ peak position measured at 15 keV with a TAP monochromator as a function of the total Fe concentration for a series of Fe^{2+}- and Fe^{3+}-bearing silicates. Numbers next to symbols in the legend indicate coordination numbers of Fe ions for minerals in which coordination numbers are not six. Error bars are given for an uncertainty of ± 8 sin increments on the Fe$L\alpha$ peak position. Below 5 wt% Fe, plots represent the average of three peak searches to fit within the latter uncertainty. All data were collected over a few months period. To correct for any deviation due to mechanical drifts of the spectrometers with time, each measurement was performed relative to the peak position of Fe_2O_3. Ln curves have no physical justification.

the site geometry can be detected from the variations of the Fe$L\alpha$ peak position, at least for silicates containing either Fe^{2+} or Fe^{3+}.

The calculated L_3 absorption spectra for Fe^{3+} and Fe^{2+} exhibit a major peak with one low-energy satellite (often called pre-peak) and one or more high-energy satellites (Cressey et al. 1993). The relative peak energies and heights depend on the crystal-field splitting termed 10Dq. In silicates, 10Dq is taken as 1.0 or 1.5 eV for fitting experimental spectra where Fe^{2+} and Fe^{3+} are in octahedral and tetrahedral sites. For either of these values of 10Dq, the overall L_3 absorption bands of Fe^{2+} and Fe^{3+} are little changed (either in maximum position or in shape) for both sites. We can reasonably expect that, given the limited resolution of the EMP, details of the *L*-absorption edge structure reflecting cation coordination vanish into the total emission signal.

Once the Fe concentration of a silicate phase has been measured by classical EMP analyses using the Fe$K\alpha$ peak [and not Fe$L\alpha$, which is not recommended for analyses of the first row transition metals (Pouchou and Pichoir 1985; Fialin et al. 1993)], $Fe^{3+}/\Sigma Fe$ can be roughly estimated in Figure 3 by comparing the measured Fe$L\alpha$ peak position to both Fe^{2+} and Fe^{3+} curves at a given Fe concentration assuming a linear increase of $Fe^{3+}/\Sigma Fe$ between both curves. Values of $Fe^{3+}/\Sigma Fe$ will be then reduced from plots giving the peak positions relative to the Fe^{2+}-Fe^{3+} curves of Figure 3 as a function of the nominal $Fe^{3+}/\Sigma Fe$ for a series of reference minerals and glasses (Fig. 4a). The total Fe concentration of reference samples used in Figure 4a is given in Figure 4b (using the same x-axis and same symbols as in Fig. 4a). In Figures 4a and 4b, full symbols represent data for glasses, garnets, and Al-rich spinels. Significant deviation from a linear relationship exists for full symbols, which shows that the position of the Fe$L\alpha$ peak in a given phase is not a linear function of $Fe^{3+}/\Sigma Fe$. Open symbols in Figure 4a represent pyroxenes, amphiboles, and micas. For a given $Fe^{3+}/\Sigma Fe$, and particularly for values far from the end-members, we observe an overall shift of open symbols relative to full symbols toward the right-end of the x-axis. Comparison of Figures 4a and 4b shows that the shifted positions of the open symbols is not related to the total Fe concentration of the corresponding samples. This deviation for open symbols corresponds to a shift of the peak maximum toward shorter wavelength, which can be interpreted as a reduction of the self-absorption for the Fe$L\alpha$ peak. In chain and sheet silicates (e.g., pyroxenes, amphiboles, and micas), mixing of the Fe-3d orbitals occurs between Fe cations of edge- and face-sharing FeO_6 polyhedra (to form metal-metal bonding by IVCT) with thermally activated transfer of an electron (electron hopping) over two or more adjacent Fe^{2+} and Fe^{3+} sites (Sherman 1987a). The IVCT mechanisms lead to the partial delocalization of the d-orbitals and thus to the reduction of the self-absorption for the $L\alpha$ peak. Broadening of the experimental Fe^{2+} L_3-absorption band in amphiboles has been reported by Cressey et al. (1993), which may reveal such a delocalization for the Fe^{2+} d-orbitals. On the other hand, IVCT is not described for minerals in which either Fe^{2+} or Fe^{3+} occupy non-sixfold coordinated sites such as garnets (eightfold coordination of Fe^{2+}) and Al-rich spinels (fourfold coordination of Fe^{2+}). For these minerals, no IVCT induced peak shift is expected. Similar conclusions hold for glasses for which recent XANES spectra obtained from basaltic glasses are consistent with mainly fourfold coordination of Fe, with the possible presence of fivefold coordination (Wu et al. 1998, 1999; Jackson et al. 1993; Brown et al. 1995).

Accuracy and precision

First, the accuracy of the method strongly depends on the nominal values of $Fe^{3+}/\Sigma Fe$ of the standards used. The scattering of data in Figure 4 may be caused in part by some problems of aggregating errors due to stoichiometry based calculation of $Fe^{3+}/\Sigma Fe$ in minerals (Sobolev et al. 1999). As a result, calibration curves should be constructed with data collected either from international references or from carefully selected samples in which $Fe^{3+}/\Sigma Fe$ was measured by wet chemical or Mössbauer methods. Second, accuracy also may be altered as a result of the sensitivity of the self-absorption of Fe$L\alpha$ to the extent of d-orbital delocalization for the absorbing ions. Two major contributions influence self-absorption in this way: (1) IVCT for mixed valence sheet and chain silicates; and (2) differences in bonding environment, for glasses in particular, due to extremely distorted cation sites and presence of other anions (OH^-, F^- etc.).

The level of precision is directly related to the uncertainty in the absolute peak position (parameter $\sin\theta_X$ in Fig. 4a). To improve the uncertainty in the peak position after a single au-

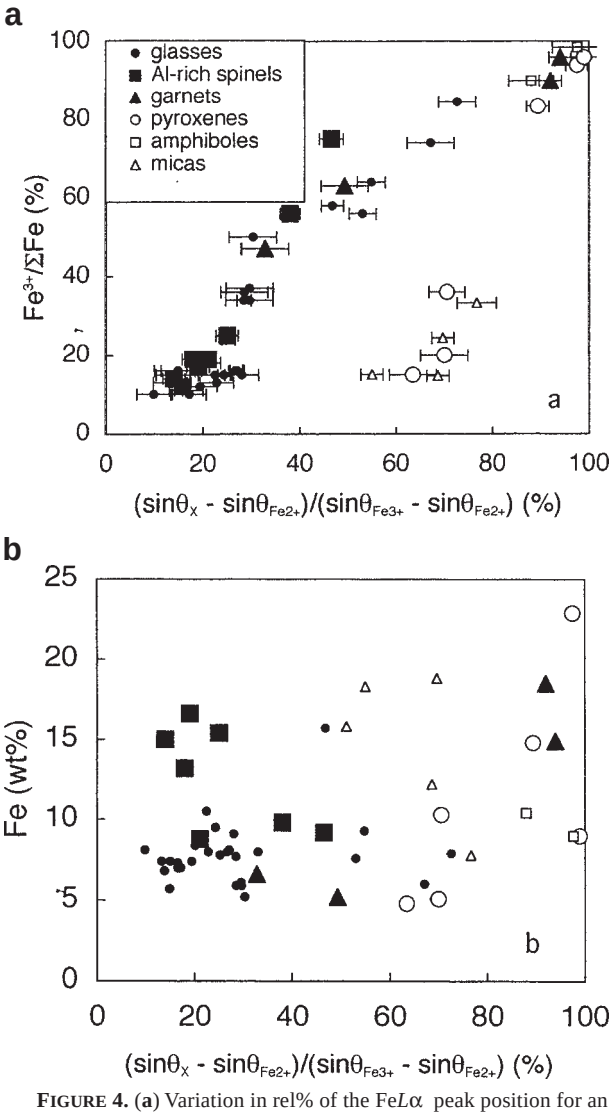

FIGURE 4. (**a**) Variation in rel% of the Fe$L\alpha$ peak position for an unknown X, relative to the separation of the Fe^{3+}-Fe^{2+} curves for the corresponding Fe content in Figure 3 (see text), as a function of the nominal $Fe^{3+}/\Sigma Fe$ for a series of reference phases. Nominal $Fe^{3+}/\Sigma Fe$ values were measured by wet chemistry for glasses, micas, and amphiboles, and deduced from the EMP analyses for other minerals (plots for the latter correspond to large full or open symbols). Open symbols represent mixed valence chain and sheet silicates that are sensitive to IVCT mechanisms (see text). Error bars (1 standard deviation) correspond to the precision achieved for the relative peak position $(\sin\theta_X\text{-}\sin\theta_{Fe2+})/(\sin\theta_{Fe3+}\text{-}\sin\theta_{Fe2+})$, provided a precision of ±3 sin increments for the absolute peak position sin $_X$. The size of the error bars are dependent on the total Fe concentrations of reference samples, which are given in (**b**). Following values for the error bar lengths can be remembered: ±5, ±3, and ±2 for 5, 8, and 15 wt% Fe, respectively.

tomated peak search (i.e., ±8 sinθ increments), the current protocol for measuring the position of the Fe$L\alpha$ peak consisted of averaging 36 peak searches. Three different sites were selected on the sample surface for these measurements (to limit both beam damage and carbon contamination), and six peak searches were carried out on each site simultaneously by two spectrometers equipped with TAP monochromators. The beam was set to 130 nA and 30 μm (see next section for justifications of these beam parameters). For these conditions, the precision achieved for $\sin\theta_X$ was ±3 sinθ increments (1σ standard deviation). Another source of error for data in Figure 4a is the uncertainty in the values of $\sin\theta_{Fe2+}$ and $\sin\theta_{Fe3+}$ that are deduced from the Ln fit curves of Figure 3. The subsequent systematic error on the relative peak position $(\sin\theta_X\text{-}\sin\theta_{Fe2+})/(\sin\theta_{Fe3+}\text{-}\sin\theta_{Fe2+})$ is not easy to evaluate but it is assumed to be low compared to errors due to the lack of statistical accuracy on $\sin\theta_X$. Finally, the error on $(\sin\theta_X\text{-}\sin\theta_{Fe2+})/(\sin\theta_{Fe3+}\text{-}\sin\theta_{Fe2+})$ is also dependent on the total Fe content of the sample through the parameter $(\sin\theta_{Fe3+}\text{-}\sin\theta_{Fe2+})$. The higher the Fe content, the higher the value of $(\sin\theta_{Fe3+}\text{-}\sin\theta_{Fe2+})$ and, thus, the lower the error propagated to $(\sin\theta_X\text{-}\sin\theta_{Fe2+})/(\sin\theta_{Fe3+}\text{-}\sin\theta_{Fe2+})$ by the uncertainty on $\sin\theta_X$. For basaltic glasses containing, on average, 8 wt% Fe and 10% $Fe^{3+}/\Sigma Fe$, a precision of ±3 sinθ increments for $\sin\theta_X$ corresponds to 6% of the separation of the Fe^{2+}-Fe^{3+} curves for 8 wt% Fe (90 sinθ increments) in Figure 3. In terms of uncertainty in $Fe^{3+}/\Sigma Fe$, ±3% (absolute) is an upper limit corresponding to a 1:1 relationship between $Fe^{3+}/\Sigma Fe$ and $(\sin\theta_X\text{-}\sin\theta_{Fe2+})/(\sin\theta_{Fe3+}\text{-}\sin\theta_{Fe2+})$ (Fig. 4). For glass data below 20% $Fe^{3+}/\Sigma Fe$, the more realistic value of 0.70:1 for the $Fe^{3+}/\Sigma Fe$ - $(\sin\theta_X\text{-}\sin\theta_{Fe2+})/(\sin\theta_{Fe3+}\text{-}\sin\theta_{Fe2+})$ relationship gives an uncertainty of about ±2% (absolute) for $Fe^{3+}/\Sigma Fe$.

LIMITATIONS

Some limitations associated with the method should be examined. The first one concerns species with low concentrations of iron (<3.5 wt% Fe) for which the method is not applicable. An uncertainty of ± 3 sinθ increments represents 20% of the separation of the Fe^{2+}-Fe^{3+} curves for 3.5 wt% Fe in Figure 3, which is propagated as prohibitively large error bars for the relative peak position $(\sin\theta_X\text{-}\sin\theta_{Fe2+})/(\sin\theta_{Fe3+}\text{-}\sin\theta_{Fe2+})$ (±10% absolute). The second limitation involves self-absorption-induced deformations of Fe$L\alpha$ that also depend on the absorption by other components of the matrix and mean atomic number of the sample as well. Indeed the higher both of the latter parameters are, the lower the escape depth of the measured Fe$L\alpha$ photons and thus the lower the self-absorption they experience. This situation is illustrated in Figure 5, where data collected from two Cr-rich spinels (SP1, SP2) and one pseudobrookite (PSB) are plotted and compared with plots of Figure 4a representing Al-rich spinels with $Fe^{3+}/\Sigma Fe$ ranging from 15 to 25%. Chromium and Ti are very absorbing elements for Fe$L\alpha$, and plots corresponding to the Cr- and Ti-rich phases lead to overestimated $Fe^{3+}/\Sigma Fe$ values as a consequence of the reduced Fe$L\alpha$ peak shift toward longer wavelength for these minerals.

The total absorption $(\mu/\rho)_t$ experienced by Fe$L\alpha$ at 15 keV in most silicates and glasses—for which the mean atomic number Z is between 10 and 15—ranges from 10000 to 15 000 cm^2/g (corresponding to escape depths ranging from 1 to 3 μm for Fe$L\alpha$). Any phase with $(\mu/\rho)_t$ and/or Z outside these ranges require specific treatments. This is the case of SP1, SP2, and PSB for which Z is between 16.5 and 18 and $(\mu/\rho)_t$ is between 20 000 and 22 000 cm^2/g (escape depths below 0.5 μm for Fe$L\alpha$). Simple iron oxides (e.g., FeO, Fe_3O_4, Fe_2O_3) with high-

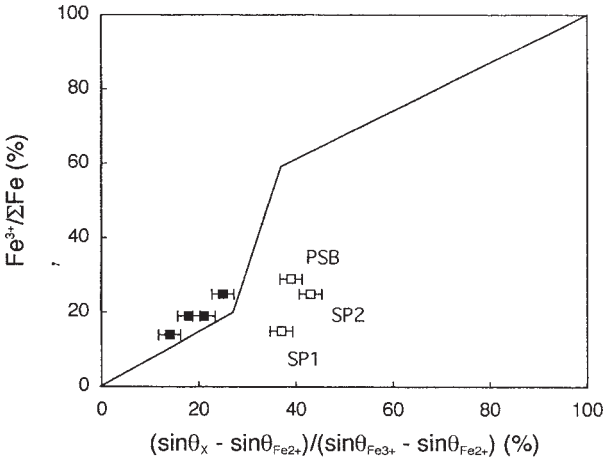

FIGURE 5. Deviations observed in the range 15–30% $Fe^{3+}/\Sigma Fe$ between Al-rich spinels (filled symbols) and Cr- and Ti-rich oxides (open symbols): spinels SP1 and SP2 with 56 and 53 wt% Cr_2O_3, respectively (to be compared with concentrations below 1 wt% for the Al-rich spinels); pseudobrookite with 70 wt% TiO_2. Due to the presence of the highly absorbing and heavy elements Cr and Ti, SP1, SP2 and PSB exhibit large total absorption coefficients $(\mu/\rho)_t$ for Fe*L*α (above 20 000 cm^2/g) and large average atomic numbers *Z* (above 17). Values of $(\mu/r)_t$ and *Z* for the Al-rich spinels are around 12 500 cm^2/g and 12, respectively. Reduced Fe*L* peak shifts toward longer wavelengths for transition-element-rich minerals lead to overestimated $Fe^{3+}/\Sigma Fe$. The solid line a rough fit of the filled symbol plots in Figure 4a. This diagram shows the complexity of the relationship between $Fe^{3+}/\Sigma Fe$ and the relative peak position $(\sin\theta_X-\sin\theta_{Fe2+})/(\sin\theta_{Fe3+}-\sin\theta_{Fe2+})$, which is far from a 1:1 line, and the large descrepancies induced on $Fe^{3+}/\Sigma Fe$ by using the latter relationship for high-Z and high $(\mu/\rho)_t$ minerals.

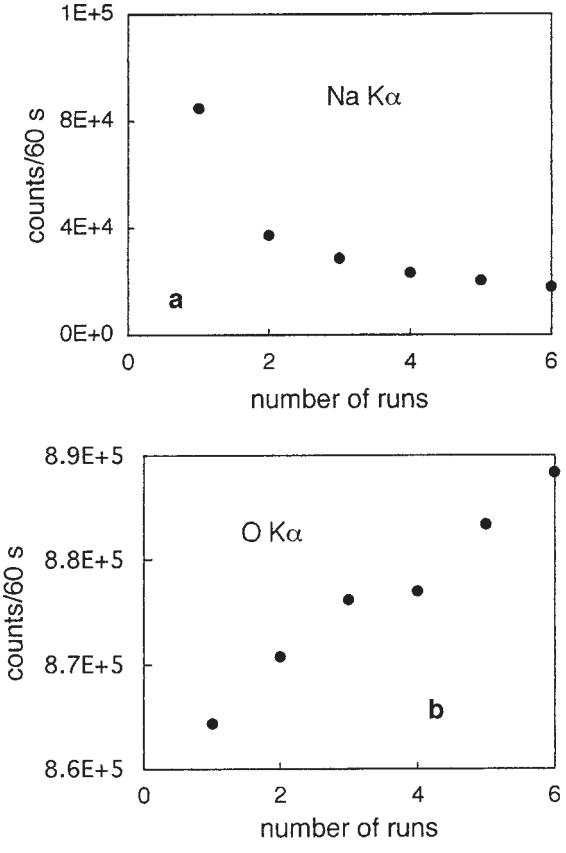

FIGURE 6. (**a**) Na*K*α intensity loss in basaltic glass (4.11 wt% Na_2O) as a function of six 60 s -integrated count runs performed on the same surface site; 60 s correspond to the time required for a single automatic peak search with the Cameca EMP. Beam conditions: 15 keV 130 nA, 10 m. (**b**) Concurrent increase of O*K* in accordance with the model of Lineweaver (1963).

Z (typically around 20) and a low absorbing matrix for Fe*L*α [$(\mu/\rho)_t$ < 10 000 cm^2/g] represent specific materials that exhibit reduced escape depths for Fe*L*α (around 0.7 μm).

Beam damage is the last but essential point to be discussed. Glasses are generally more beam sensitive than minerals, and they are known to be affected by oxygen as well as alkali ion migration under electron bombardment (see review by Morgan and London 1996). This phenomenon is illustrated for a tholeiitic glass in Figure 6 where plots for O and Na were acquired simulteanously on two spectrometers with 60 s counting time. The enrichment in oxygen of the surface layers causes the Fe*L*α peak to shift toward shorter wavelength. This shift was revealed by completing six consecutive peak searches on a single surface site of the basaltic glass at 15 keV, 130 nA, and with varying beam diameter. Results are presented in Figure 7 where linear fits to experimental plots are shown. The increase in slope as the beam diameter is reduced from 20 to 10 μm reflects enhanced surface oxidation kinetics. For 30 and 5 μm, the peak position varies slowly, which would indicate weak beam damage for both operating conditions. Actually for 5 μm, the time constant of the surface oxidation kinetics is so short that the peak is shifted rapidly (probably far before the first peak search run was completed), which provides unexpected high values for $Fe^{3+}/\Sigma Fe$. For 30 μm, the primary electron dose is not large enough to produce noticeable effects. Surface oxidation kinetics are accompanied by common glass alterations such as electron browning and surface displacement in the direction of bombarding electrons (Lineweaver 1963). To prevent beam damage, measurements on most glasses studied here were performed at 15 keV, 130 nA, and 30 μm for which no significant peak shifts were measured with increasing irradiation time, at least over the total time required for six peak searches (i.e., 360 s).

PERSPECTIVES AND CONCLUSIONS

The technique described in this paper holds promise for $Fe^{3+}/\Sigma Fe$ measurements at the micrometer scale with the EMP using the self-absorption-induced shift of the Fe*L*α peak. The technique is applicable to silicates and glasses with total Fe concentration above 3.5 wt%. The next step in the study is the construction of calibration curves, which necessitates further wet-chemical and Mössbauer analyses to increase the number of data points in Figure 4. The technique can be applied to oxides and especially those with large concentrations of Ti, Cr, and Mn (all elements that are strong absorbers of Fe*L*α), for which other sets of calibration curves should be established. Furthermore, for transition-element-rich minerals, we expect serious difficulties with IVCT mechanisms, especially for Fe-

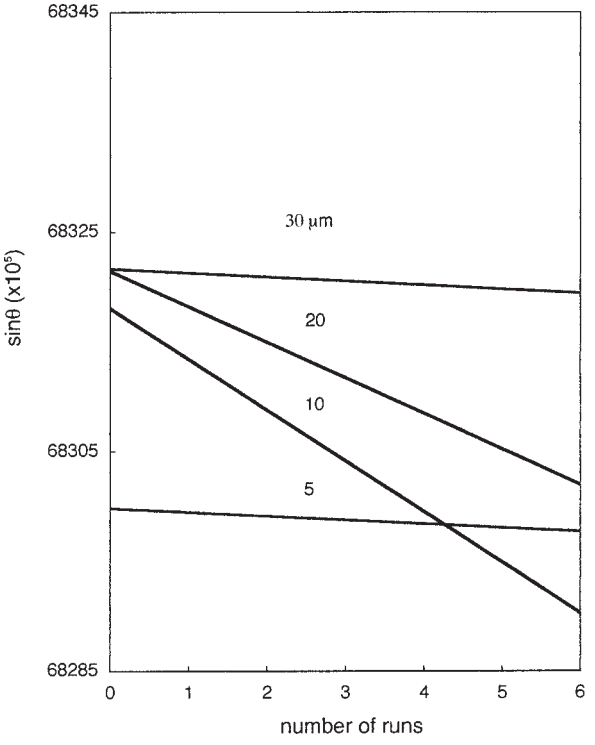

FIGURE 7. Beam irradiation induced Fe*L*α peak shift for the basaltic glass of Figure 6. Beam conditions: 15 keV, 130 nA, varying beam diameter (given in micrometers above curves). Values on the x-axis are the same as Figure 6. Experimental plots are omitted for the clarity of the figure. Curves represent linear fits to plots. Extrapolation to run 0 shows the theoretical unaltered position of the Fe*L*α peak. For a 5 µm beam diameter, the linear fit cannot account for the rapid surface oxidation process, which leads to prohibitively large discrepancies for the estimated peak position.

and Ti-bearing (Sherman 1987b), and Fe- and Mn-bearing (Sherman 1990) minerals. The technique can also be applied to hydrated glasses (e.g., volcanic inclusion glasses) for which primary experiments have shown that beam damage is a crucial question to be studied carefully. Beam damage for hydrated glasses was already reported by application of a method based on the S*K*α peak shift for determining oxygen fugacity in individual S-bearing glasses (Métrich and Clocchiatti 1996; Clémente 1998).

The accuracy of the method is strongly dependent on (1) the sensitivity of the self-absorption of Fe*L*α to the nature and arrangement of the lattice surrounding Fe ions (matrix corrections for strong absorbers of Fe*L*α present in a sample, correction for IVCT, other currently unidentified sample-specific factors), and (2) beam damage. It is thus premature to suggest that the determination of $Fe^{3+}/\Sigma Fe$ is precise enough to be fully quantitative considering an uncertainty of about ±10% relative as an appropriate value for an analytical technique (the actual precision is ±20% relative for 10% $Fe^{3+}/\Sigma Fe$). The question remains open about the number of calibration curves needed to cover the different mineral groups and glasses.

From the instrumental point of view, the need should be stressed for high-performance, wavelength-dispersive spectrometers that measure, with good accuracy and as rapidly as possible, the position of the Fe*L*α peak emitted from phases with rather low Fe concentrations, typically below 10 wt% (which includes most silicates). Improvements need to address mainly two competing properties of the monochromator crystals, namely the reflectivity and the resolution. The TAP monochromator exhibits poor reflectivity (leading to low count rates) and would be replaced preferably by metallic multilayer monochromators (MMM). The great advantage of MMM is the possibility to adjust parameters such as the *d*-spacing, the surface size, and the couple of deposited material, to optimize the detection of a given X-ray. The fixed *d*-spacing of TAP (2.575 nm) in connection with Bragg's law force this crystal to be positionned in the spectrometer far from the X-ray source to detect Fe*L*α. Selecting enhanced *d*-spacing for the MMM would produce a reduction of the source-crystal distance with a subsequent increase of the incoming X-ray flux intercepted by the crystal. The disadvantage of this operation is the loss of resolution of the monochromator (good resolution remains essential to keep the separation large enough between both the Fe^{2+} and Fe^{3+} *L*α peak positions). To overcome this drawback, a new type of MMM has been described (Sammar et al. 1993; Fialin et al. 1996). New MMM consist of lamellar gratings etched in the multilayer structure to produce the desired bandwidth reduction by lightening the diffractive medium. The design of an MMM for improved detection of Fe*L*α is in progress.

ACKNOWLEDGMENTS

We are indebted to the following colleagues for providing part of the samples studied here and/or for constructive discussions: M.A. Arrio, M. Fonteilles, Y. Fuchs, D.R. Neuville (campus Jussieu); M. Bonnin-Mosbah, D. Massare, and R. Moretti (CE-Saclay). We also thank Heidi Höfer, Stuart Raeburn, Jeremy Delaney, and David London whose thorough reviews enhanced the quality of the manuscript.

REFERENCES CITED

Amundsen, H.E.F. and Neumann, E.R. (1992) Redox control during mantle/melt interaction. Geochimica et Cosmochimica Acta, 56, 2405–2416.

Ballhaus, C., Berry, F., and Green, D.H. (1990) Oxygen fugacity controls in the earth's upper mantle. Nature, 348, 437–440.

Bingham, P.A., Parker, J.M., Searle, T., Williams, J.M., and Fyles, K. (1999) Redox and clustering of iron in silicate glasses. Journal of Non-Crystalline Solids, 253, 203–209.

Bonnelle, C. (1966) Contribution à l'étude des métaux de transition du premier groupe, du cuivre et de leurs oxydes par spectroscopie X dans le domaine de 13 à 33 Å. Thesis p 1–43, Masson, Paris.

———(1987) X-ray spectroscopy. Annual Report C, p. 201–272. The Royal Society of Chemistry, London.

Brown, G.E., Farges, F., and Calas, G. (1995) X-ray scattering and x-ray spectroscopy studies of silicate melts. In J.F. Stebbins, P.F. McMillan, and D.B. Dingwell, Eds., Structure, Dynamics, and Properties of Silicate Melts, 32, p. 317–410. Mineralogical Society of America, Reviews in Mineralogy, Washington, D.C.

Burns, R.G. (1993) Mineralogical applications of crystal field theory, second edition. In A. Putnis and R.C. Liebermann, Eds., Cambridge topics in mineral physics and chemistry. Cambridge University Press, U.K.

Canil, D., O'Neill, H., Pearson, D.G., Rudnick, R.L., McDonough, W.F., and Carswell, D.A. (1994) Ferric iron in peridotites and mantle oxidation states. Earth and Planetary Science Letters, 123, 205–220.

Christie, D.M., Carmichael, I.S.E., and Langmuir, C.H. (1986) Oxidation states of mid-ocean ridge basalt glasses. Earth and Planetary Science Letters, 79, 397–411.

Clémente, B. (1998) Etude expérimentale et modélisation de la solubilité du soufre dans les liquides magmatiques. Thesis p. 1–226, Orléans.

Cooney, T.F. and Sharman, S.K (1990) Structure of glasses in the systems Mg_2SiO_4-Fe_2SiO_4, Mn_2SiO_4-Fe_2SiO_4, Mg_2SiO_4-$CaMgSiO_4$ and Mn_2SiO_4-$CaMnSiO_4$. Journal of Non-Crystalline Solids, 122, 10–32.

Cressey, G., Henderson, C.M.B., and van der Laan, G. (1993) Use of L-edge x-ray

absorption spectroscopy to characterize multiple valence states of 3d transition metals; a new probe for mineralogical and geochemical research. Physics and Chemistry of Minerals, 20, 111–119.

de Groot, F.M.F. (1994) X-ray absorption and dichroism of transition metals and their compounds. Journal of Electron Spectroscopy and Related Phenomena, 67, 529–622.

de Groot, F.M.F., Fuggle, J.C., Thole, B.T., and Sawatzky, G.A. (1990) 2p x-ray absorption of 3d transition-metal compounds: An atomic multiplet description including the crystal field. Physical Review B, 42-9, 5459–5468.

Delaney, J.S., Dyar, M.D., Sutton, S.R., and Bajt, S. (1998) Redox ratios with relevant resolution: solving an old problem by using the synchrotron micro-XANES probe. Geology, 26, 139–142.

Dyar, D.M. (1985) A review of Mössbauer data in inorganic glasses: the effects of composition on iron valency and coordination. American Mineralogist, 70, 304–316.

Eibschutz, M. and Lines, M.E. (1982) Observation of second order quadrupole shift on Mössbauer spectrum of amorphous YIG (yttrium iron garnet). Physical Review, B25, 4256–4259.

Fialin, M., Hénoc, J., and Rémond, G. (1993) A survey of electron probe microanalysis using soft radiations: difficulties and presentation of a new computer program for wavelength dispersive spectrometry. Scanning Microscopy Supplement 7, 153–166.

Fialin, M., Rémy, H., André, J.M., Chauvineau, J.P., Rousseaux, F., Ravet, M.F., Decanini, D., and Cambril, E. (1996) Extending the possibilities of soft x-ray spectrometry through the etching of layered synthetic microstructure monochromators. X-ray spectrometry, 25, 60–65.

Garvie, L.A.J. and Buseck, P.R. (1998) Ratios of ferrous to ferric iron from nanometre-sized areas in minerals. Nature, 396, 667–670.

Höfer, H.E., Brey, G.P., Schulz-Dobrick, B., and Oberhänsli, R (1994) The determination of the oxidation state of iron by the electron microprobe. European Journal of Mineralogy, 6, 407–418.

Höfer, H.E., Weinbruch, S., McCammon, C.A., and Brey G.P. (2000) Comparison of two electron probe microanalysis techniques to determine ferric iron in synthetic wüstite samples. European Journal of Mineralogy, 12, 63–71.

Holliday, J.E. (1968) Soft x-ray emission bands and bonding for transition metals, solutions and compounds. In D.J. Fabian, Ed., Soft X-ray Band Spectra p. 101–132. Academic Press, London.

Humler, E., Meyzen, C., Ludden, J., and Mevel, C. (1998) Geochemical variations in basaltic glasses from the South West Indian Ridge (49 to 69° E). AGU fall meeting, EOS 79, 878.

Jackson, W.E., Brown, G.E. Jr., Waychunas, G.A., Mustre de Leon, J., Conradson, S.D., and Combes, J.M. (1990) In-situ high temperature x-ray absorption study of ferrous iron in orthosilicate crystals and liquids. In S.S. Hasnain, Ed., X-ray Absorption Fine Structure VI, p. 294–301. Ellis Horwood.

Jackson, W.E, Waychunas, G.E., Brown, G.E., Mustre de Leon, J., Conradson, S., and Combes, J.M. (1993) High temperature XAS study of Fe_2SiO_4: evidence for reduced coordination of ferrous iron in the liquid. Science, 262, 229–233.

Kadik, A.A. (1997) Evolution of Earth's redox state during upwelling of carbon-bearing mantle. Physics of Earth and Planetary Interiors, 100, 157–166.

Kadik, A.A. and Lukanin O.A. (1985) Paths for mantle outgassing during melting: change in fluid composition and conditions in basaltic magmas during migration to the surface. Int. Geol. Rev., 27, 573–586.

Kasting, J.F., Eggler, D.H., and Raeburn, S.P. (1993) Mantle redox evolution and the oxidation state of the Archean atmosphere. Journal of Geology, 101, 245–257.

Liefeld, R.J. (1968) Soft x-ray emission spectra at threshold excitation. In D.J. Fabian, Ed., Soft X-ray Band Spectra, p. 133–149. Academic Press, London.

Lineweaver, J.L. (1963) Oxygen outgassing caused by electron bombardment of glass. Journal of Applied Physics, 34(6), 1786–1791.

Mao, H.K., Virgo, D., and Bell, P.M. (1973) Analytical study of the orange soil returned by the Apollo 17 astronauts. Carnegie Institution Washington Year Book, 72, 631–638.

Mattioli, G.S., Baker, M.B., Rutter, M.J., and Stolper, E.M. (1989) Upper mantle oxygen fugacity and its relationship to metasomatism. Journal of Geology, 97, 521–536.

McCammon, C.A., Chaskar, V., and Richards, G.G. (1991) A technique for spatially resolved Mössbauer spectroscopy applied to quenched metallurgical slags. Measurement Science and Technology, 2, 657–662.

McGuire, A.V., Dyar, M.D., and Nielson, J.E. (1991) Metasomatic oxidation of upper mantle peridotite. Contributions to Mineralogy and Petrology, 109, 252–264.

Métrich, N. and Clocchiatti, R. (1996) Sulfur abundance and speciation in oxidized alkaline melts. Geochimica et Cosmochimica Acta, 60, 4151–4160.

Morgan VI, G.B. and London, D. (1996) Optimizing the electron microprobe analysis of hydrous alkali aluminosilicate glasses. American Mineralogist, 81, 1176–1185.

Mysen, B.O. (1988) Structure and properties of silicate melts. In W.S. Fyfe, Ed., Developments in Geochemistry, 4, p 146–186. Elsevier.

O'Neill, H.S.C., Rubie, D.C., Canil, D., Geiger, C.A., Ross II, C.R., Seifert, F., and Woodland, A.B. (1993) Ferric iron in the upper mantle and in transition zone assemblages: implications for relative oxygen fugacities in the mantle. In Evolution of the Earth and Planets, International Union of Geodesy and Geophysics and the American Geophysical Union, Geophysical monograph 74, IUGC Vol. 14, 73–88.

O'Nions, R.K. and Smith, D.G.W. (1971) Investigations of the $L_{II,III}$ x-ray emission spectra of Fe by electron microprobe. Part 2. The Fe $L_{II,III}$ spectra of Fe and Fe-Ti oxides. American Mineralogist, 56, 1452–1463.

Parratt, L.G. (1959) Electronic band structure of solids by x-ray spectroscopy. Reviews of Modern Physics, 31(3), 616–645.

Pouchou, J.L. and Pichoir, F. (1985) Anomalies d'émission et d'absorption du rayonnement Ni Lα. Journal de Microscopie et de Spectroscopie Electronique, 10, 291–294.

Raeburn, S.P., Ilton, E.S., and Veblen, D.R. (1997a) Quantitative determination of the oxidation state of iron in biotite using x-ray photoelectron spectroscopy: I. Calibration. Geochimica et Cosmochimica Acta, 61 (21), 4519–4530.

———(1997b) Quantitative determination of the oxidation state of iron in biotite using x-ray photoelectron spectroscopy: II. In situ analyses. Geochimica et Cosmochimica Acta, 61 (21), 4531–4537.

Rémond, G., Gilles, C., Fialin, M., Rouer, O., Marinenko, R., Myklebust, R., and Newbury, D. (1996) Intensity measurement of wavelength dispersive x-ray emission bands: applications to the soft x-ray region. Mikrochimica Acta, [Suppl.] 13, 61–86.

Sammar, A.E., André, J.M., Ouahabi, M., Pardo, B., and Barchewitz, R. (1993) Monochromateur multicouche à bande passante étroite pour le rayonnement X, Comptes Rendus de l'Académie des Sciences Paris, 316(II), 1055–1060.

Sato, M. (1970) Electrochemical measurements and control of oxygen fugacity and other gaseous fugacities with solid electrolyte systems. In G.C. Ulmer, Ed., Research Techniques for High Pressure and High Temperatures, p. 43–99. Springer, Berlin.

Sherman, D.M. (1987a) Molecular orbital (SCF-Xα-SW) theory of metal-metal charge transfer processes in minerals.I. Application to $Fe^{2+} \rightarrow Fe^{3+}$ charge transfer and « electron delocalization » in mixed-valence iron oxides and silicates. Physics and Chemistry of Minerals, 14, 355–363.

———(1987b) Molecular orbital (SCF-Xα-SW) theory of metal-metal charge transfer processes in minerals. II. Application to $Fe^{2+} \rightarrow Ti^{4+}$ charge transfer transitions in oxides and silicates. Physics and Chemistry of Minerals, 14, 364–367.

———(1990) Molecular orbital (SCF-Xα-SW) theory of Fe^{2+}-Mn^{2+}, Fe^{3+}-Mn^{2+}, and Fe^{3+}-Mn^{3+} charge tranfer and magnetic exchange in oxides and silicates. American Mineralogist, 75, 256–261.

Sobolev, V.N., McCammon, C.A., Taylor, A.T., Snyder, G.A., and Sobolev, N.V. (1999) Precise Mössbauer milliprobe determination of ferric iron in rock-forming minerals and limitations of electron microprobe analysis. American Mineralogist, 84, 78–85.

van Aken, P.A., Liebscher, B., and Styrsa, V.J. (1998) Quantitative determination of iron oxidation states in minerals using Fe $L_{2,3}$-edge electron energy-loss near-edge structure spectroscopy. Physics and Chemistry of Minerals, 25, 323–327.

van Aken, P.A., Styrsa, V.J., Liebscher, B., Woodland, A.B., and Redhammer, G.J. (1999) Microanalysis of $Fe^{3+}/\Sigma Fe$ in oxide and silicate minerals by investigation of electron energy-loss near-edge structures (ELNES) at the $M_{2,3}$ edge. Physics and Chemistry of Minerals, 26, 584–590.

Virgo, D., Luth, R.W., Moats, M.A., and Ulmer, G.C. (1988) Constraints on the oxidation state of the mantle: an electrochemical and ^{57}Fe Mössbauer spectroscopy and resultant oxygen fugacities. Geochimica et Cosmochimica Acta, 53, 1781–1794.

Waychunas, G.A., Brown, G.E. Jr., Ponader, C.W., and Jackson, W.E. (1988) Evidence from x-ray absorption for network-forming Fe^{2+} in molten alkali silicates. Nature, 332, 251–253.

Westre, T.A., Kennepohl, P., DeWitt, J.G., Hedman, B., Hodgson, K.O., and Solomon, E.I. (1997) A multiplet analysis of Fe K-edge 1s → 3d pre-edge features of iron complexes. Journal of the American Chemical Society, 119, 6297–6314.

Wilson, A.D. (1960) Micro-determination of ferrous iron in silicate minerals by a volumetric and a calorimetric method. Analyst, 85, 823–827.

Wood, B.J., Bryndzia, T., and Johnson, K.E. (1990) Mantle oxidation state and its relationship to tectonic environment and fluid speciation. Science, 248, 337–344.

Wu, Z.Y., Bonnin-Mosbah, M., Duraud, J.P., Métrich, N., and Delaney, J.S. (1998) Study of redox state of iron and structure of natural basaltic glasses by μ-XANES. AGU fall meeting, EOS 79, 954.

———(1999) XANES studies of Fe-bearing glasses. Journal of Synchrotron Radiations, 6, 344–346.

MANUSCRIPT RECEIVED APRIL 11, 2000
MANUSCRIPT ACCEPTED DECEMBER 14, 2000
MANUSCRIPT HANDLED BY DAVID LONDON